Article

Machine Learning Interatomic Potentials for Modeling Framework Flexibility and Water Uptake in NbOFFIVE-1-Ni Metal−Organic Framework

Xijun Wang,[#] Xiaoliang Wang,[#] Xiaoyi Zhang, Zhao Li, Jiayang Liu, Faramarz Joodaki, Kaihang Shi, Filip Formalik, Omar K. Farha, Daniela Kohen, and Randall Q. Snurr*

Cite This: https://doi.org/10.1021/acs.jpcc.6c00023

Read Online

ACCESS | Metrics & More | Article Recommendations | Supporting Information

ABSTRACT: Metal−organic frameworks (MOFs), with their distinctive porous structures and tunable chemical properties, have shown immense promise in the separation and storage of gases. Currently, the accurate simulation of their adsorptive properties remains challenging, especially for systems where the molecules fit very tightly into the pores. Traditional simulation methods often approximate the frameworks as rigid and do not account for the framework flexibility seen in materials such as NbOFFIVE-1-Ni. First-principles molecular dynamics (FPMD) simulations offer the desired accuracy in modeling this flexibility but are limited by their extensive computational demands, rendering them impractical for long simulations. Conversely, classical force field-based simulations offer computational efficiency but lack the necessary accuracy. To break this accuracy-efficiency trade-off, we have developed machine learning interatomic potentials trained on energies and forces from FPMD to model the framework flexibility of NbOFFIVE-1-Ni in the presence of water over nanosecond time scales. Furthermore, by integrating MLIP-driven molecular dynamics (MLIP-MD) with grand canonical Monte Carlo (GCMC) simulations, we further incorporated framework flexibility into adsorption predictions, yielding water adsorption isotherms that better align with experimental data compared to those of conventional GCMC simulations. These advances offer new opportunities for the design and optimization of MOFs in gas storage and separation applications.
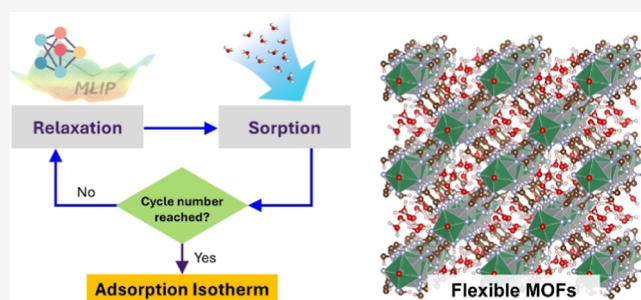
1. INTRODUCTION

Metal−organic frameworks (MOFs) are porous crystalline materials resulting from the self-assembly of inorganic nodes and organic linkers.[1] Their exceptionally high surface area, tunable chemistry, and structural versatility make them promising candidates for diverse applications, including gas storage,[2] separation,[3] catalysis,[4] and sensing.[5] In many applications, water adsorption has a significant impact on the performance or on the stability of the MOF. For example, in direct air capture of CO_2, water can compete for adsorption sites, alter the structural conformation of the MOF, and modify host−guest interactions, ultimately impacting CO_2 uptake.[6,7] Similarly, in atmospheric water harvesting and humidity control, MOFs with high water uptake capacity enable efficient capture and release of water under varying environmental conditions, providing potential solutions for water scarcity.[8,9]

Many MOFs exhibit guest-responsive flexibility, such as breathing,[10] swelling,[11] and linker rotations,[12] which can significantly impact the adsorption capacity and selectivity. Materials such as MIL-53,[13] CALF-20,[14] and CAU-10-H[15] exhibit such dynamic behavior. NbOFFIVE-1-Ni is a flexible MOF where framework dynamics play a crucial role in adsorption behavior (Figure 1).[16,17] This material has demonstrated interesting water and CO_2 adsorption behavior, which has been attributed to its strong host−guest interactions and the ability of its linker to rotate in response to water molecules.[16,18] Understanding the flexibility of such materials and their influence on adsorption, particularly in response to water, is essential for future material design and optimization.

Computational modeling has become an essential tool in MOF research, reducing costly experimental trial-and-error efforts and accelerating the discovery of high-performance materials.[19−21] However, accurately modeling flexible MOFs, especially their interplay with guest molecules, remains a significant challenge. One of the primary challenges involves efficiently and accurately obtaining system energies during molecular simulations such as molecular dynamics (MD) simulations. Classical force field-based MD, while computa-
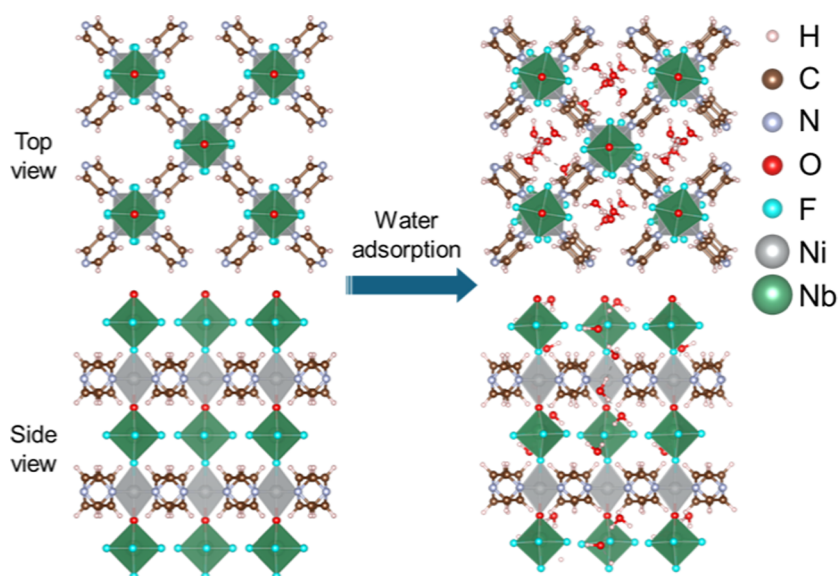
Figure 1. Unit cell of the NbOFFIVE-1-Ni framework without H_2O uptake (left) and with 12 H_2O molecules (right).

tionally efficient, lacks the accuracy required to capture strong noncovalent and coordination interactions, especially the strong interactions between transition metal sites and surrounding atoms. Although some studies have successfully applied custom-developed force fields to model adsorption in flexible MOFs,[22−25] these force fields often require extensive parametrization and exhibit limited transferability across different systems, restricting their broader applicability. In contrast, first-principles molecular dynamics (FPMD) simulations provide highly accurate simulations but are computationally prohibitive for larger time and length scale simulations due to their intensive computational cost. A promising recent advancement aimed at bridging this gap is the development of machine-learning interatomic potentials (MLIPs),[26] which have been increasingly applied to MOF systems.[27−30] Trained on density functional theory (DFT) or FPMD data, MLIPs can effectively learn the potential energy surface and accurately capture structure-energy-force relationships, thereby achieving near-DFT accuracy with a significantly reduced computational cost. This approach enables high-fidelity, large-scale simulations that were previously infeasible due to computational limitations.

Another major challenge lies in accurately sampling the dynamic structural changes of MOFs during adsorption, which is particularly critical for flexible MOFs. Traditional grand canonical Monte Carlo (GCMC) simulations typically assume a rigid framework and thus often fail to capture the structural flexibility of MOFs, resulting in considerable discrepancies between the simulated and experimental adsorption isotherms. For instance, previous work by Daglar et al.[18] employed GCMC simulations to calculate the water adsorption isotherm of NbOFFIVE-1-Ni using the DFT-optimized MOF structure. However, this approach significantly underestimated water uptake compared to experimental results, predicting a maximum adsorption of only 4 mol/kg (8 H_2O molecules per unit cell) under 80% relative humidity (RH) at room temperature, whereas the experimental value reached 6 mol/kg (12 H_2O molecules per unit cell). To improve accuracy, that study also employed DFT to sample a series of structures corresponding to different water uptake levels, resulting in adsorption isotherms that more closely matched previous

experimental data.[16] However, this limited sampling approach could not fully capture the extent of the dynamic framework flexibility.

To more efficiently sample configurations that account for framework flexibility, previous studies have explored hybrid MD and GCMC approaches.[31−33] For instance, Colina et al. proposed a sorption-relaxation (SR) workflow to study gas adsorption in flexible polymeric materials.[31] Their workflow iteratively combines classical force field-based MD simulations, which account for polymer chain rearrangement, swelling, and plasticization, with GCMC simulations to predict the adsorbate uptake for the MD-relaxed structures. This approach highlights the advantages of hybrid MD and MC methods in enhancing the sampling efficiency for flexible materials.

In this work, we trained an MLIP on FPMD-generated structures to systematically investigate the framework flexibility of NbOFFIVE-1-Ni in the presence of adsorbed water. This approach enabled MD simulations with near-DFT accuracy for systems exceeding 1000 atoms, extended simulation times to the nanosecond scale, and achieved computational efficiency 4 orders of magnitude faster than FPMD. We also employed MLIP-MD in the relaxation module of the SR workflow, enabling systematic sampling of hydrated framework structures when predicting adsorption isotherms. Compared to traditional GCMC with a rigid framework, this hybrid approach samples the framework flexibility, yielding water adsorption isotherms that align more closely with experimental data measured as part of this work, especially at low relative humidity. While the SR approach does not fully reproduce the sharp adsorption steps observed experimentally, it nonetheless offers a clear improvement over traditional rigid-framework methods. The remaining discrepancies between simulation and experiment in the NbOFFIVE-1-Ni system highlight opportunities for further development, and this work paves the way for future advances in the modeling of complex sorption phenomena.

2. COMPUTATIONAL AND EXPERIMENTAL METHODS

2.1. Model Creation and Structural Modeling

The structure of NbOFFIVE-1-Ni (as-made composition: [Ni-(NbOF$_5$)-(C$_4$H$_4$N$_2$)$_2$·2H$_2$O]),[16] also known as KAUST-7, was obtained from the Cambridge structural database (deposition no. 1505385). In the experimental structure, the fluorine (F) and oxygen (O) anion sites in (NbOF$_5$)$^{2-}$ are partially occupied, with an O/F ratio of 1:5, leading to multiple possible structural configurations. To address this, we manually assigned the F and O atoms based on the chemical composition of NbOFFIVE-1-Ni and constructed two structural models by varying the arrangement of O and F atoms within the (NbOF$_5$)$^{2-}$ units, as illustrated in Figure S1.

To assess the impact of structural variation on adsorption behavior, we performed DFT optimizations followed by GCMC simulations using the methods described in Sections 2.2 and 2.4 for both configurations. The resulting water adsorption isotherms exhibited negligible differences (Figure S2), indicating that either structure could be used for subsequent simulations. For consistency, we selected one configuration (Model A in Figure S1) as the representative model for further computational studies (Figure 1).

2.2. DFT and FPMD Simulations

Structural optimizations and FPMD simulations were carried out using spin-polarized DFT, as implemented in the Vienna Ab Initio Simulation Package (VASP).[34] The projector augmented wave (PAW) method[35] was employed in conjunction with the Perdew–Burke–Ernzerhof (PBE) exchange-correlation functional.[36] The plane-wave energy cutoff was set to 500 eV, ensuring a balance between computational efficiency and accuracy. The maximum force convergence criterion for geometry optimization was set to 0.01 eV/Å, and the energy difference convergence criterion for the SCF cycles was set to 10^{-5} eV. Brillouin zone sampling was performed by using only the Gamma point. To account for dispersion interactions, a van der Waals correction was included using the DFT-D3(BJ) method.[37]

Unless otherwise specified in the text, the FPMD simulations in VASP were conducted within the NVT ensemble, where the number of atoms (N), volume (V), and temperature (T) were held constant. A Nosé–Hoover thermostat[38,39] was used to maintain the system temperature at 300 K. The atomic trajectories were propagated using Newton's equations of motion with a time step of 1 fs, which has been shown to be suitable for generating frames for MLIP training.[40,41] To more easily view the results, a time-integrated sliding window approach was used to compute the moving average of the system's total energy. The averaged energy, $\overline{E}(t)$, was calculated using the following equation:[42]

$$\overline{E}(t) = \frac{1}{\Delta t} \int_{t}^{t+\Delta t} E(\tau) d\tau \tag{1}$$

where $E(\tau)$ is the instantaneous energy at time τ and Δt is the window size, which was set to 400 fs.

2.3. MLIP Training and MLIP-MD Simulations

The DeePMD-kit package[43,44] was employed to train a MLIP that learns the relationships between atomic positions, total energy, and atomic forces from FPMD trajectory data. In this approach, the total system energy is expressed as the sum of individual atomic contributions, which are functions of the local atomic environment. To accurately represent the local environment, DeePMD-kit utilizes two neural networks: an embedding network and a fitting network.[43] The embedding network constructs local descriptors by encoding atomic interactions and incorporating both radial and angular information. These descriptors serve as input to the fitting network, which predicts atomic forces and total energies based on the learned representations. This two-step process allows the model to capture complex structure-energy-force relationships while maintaining computational efficiency.

For our study, the embedding network consisted of three hidden layers with 25, 50, and 100 neurons, mapping the local atomic

environment matrix (constructed from atomic coordinates) to the corresponding descriptor matrix. The se_e2_a descriptor was employed, where "e2" indicates that two-body interactions (interatomic distances) were included, and "a" denotes the incorporation of both angular and radial features.[43] The neighbor cutoff radius was set to 8.0 Å to define the local atomic environment, ensuring that all relevant neighboring atomic interactions were included in the descriptor matrix. The fitting network, responsible for mapping the descriptor matrix to total energy and atomic force predictions, was designed with 3 hidden layers of 100 neurons each. The training objective was to minimize a loss function $L(p_e, p_f)$ that balances energy and force components:[43]

$$L(p_e, p_f) = \frac{p_e}{N} \Delta \epsilon^2 + \frac{p_f}{3N} \sum_i (\Delta F_i)^2 \tag{2}$$

where $\Delta \epsilon$ denotes the difference between the predicted and reference total energy, and ΔF_i denotes the difference between the predicted and reference atomic forces for atom i. The parameters p_e and p_f control the relative weight of the energy and force errors, respectively. To ensure an appropriate balance between energy and force accuracy, we applied a dynamic weighting scheme in DeePMD-kit.[44] The energy prefactor p_e was initially set to 0.02 and gradually increased to 1, while the force prefactor p_f decreased from 1000 to 1. This adaptive approach ensures that the model initially prioritizes accurate force predictions, facilitating better structural relaxation before gradually shifting the focus toward improving the energy accuracy. This strategy has been reported to be reliable for balancing accuracy and computational efficiency during training and evaluation.[45] The learning rate followed an exponential decay schedule, starting at 0.001 and decreasing to 3.51 × 10^{-8} over 1,000,000 training steps. These values are recommended for DeePMD-kit training to ensure stable convergence.[44,46] An adaptive batch size was used, and validation was performed every 1000 steps, with model checkpoints saved every 10,000 steps. A random seed of 10 was applied to ensure reproducibility. All the training data and obtained MLIPs can be accessed on Zenodo.[47]

The MLIP-driven MD (MLIP-MD) simulations were implemented in LAMMPS.[48] Periodic boundary conditions were applied in all three directions. The MLIP was incorporated using the *pair_style deepmd* command, ensuring that all atomic interactions were governed by the MLIP. The system was thermalized using an NVT ensemble using a Nosé–Hoover thermostat,[38,39] maintaining a constant temperature of 300 K with a relaxation time (also called temperature damping parameter) of 0.04 ps. Initial atomic velocities were generated to reproduce the Maxwell distribution at 300 K with a random seed. A time step of 1 fs was used for numerical integration with the Velocity–Verlet algorithm.[49] Throughout the simulations, key system properties, including potential energy, kinetic energy, total energy, temperature, and pressure, were monitored and output at every step. Atomic coordinates were recorded every 100 steps.

In Section 3.4, we describe MLIP-MD simulations in the NPT ensemble that were conducted for comparison purposes, allowing the framework volume to dynamically adjust under a constant pressure. The isotropic pressure was set to the value corresponding to each humidity level (see Section 2.4 and Table S2 for the specific pressure and RH values sampled in this work), using a barostat damping parameter of 1.0 ps.

2.4. GCMC Simulations

All GCMC simulations were performed using gRASPA,[30] a GPU-accelerated Monte Carlo simulation code. The Lennard–Jones (LJ) 12−6 potential was used to describe nonbonded dispersion and repulsion interactions. For both water–water and water-framework Lennard–Jones interactions, a cutoff distance of 9.7 Å was used; tail corrections were applied to the water–water interactions. LJ parameters for framework atoms were taken from the universal force field (UFF),[50] and the Lorentz–Berthelot mixing rules were used to obtain LJ parameters between different pseudoatoms.[51] Long-range Coulombic interactions were calculated using the Ewald

summation with a precision of 10^{-6}.[52] Periodic boundary conditions were applied in all three dimensions by using a $2 \times 2 \times 2$ supercell with lattice parameters $a = b = 19.64$ and $c = 31.49$ Å. To assign partial charges to the framework atoms, we used the density derived electrostatic and chemical (DDEC06) method.[53,54]

Water was modeled using the rigid, 4-site TIP4P model,[55] which has been shown to provide a more accurate estimation of the saturated vapor pressure compared to other commonly used water models.[56] In this model, $a -1.04e$ charge on the center of mass (L-H_2O) site and $+0.52e$ charges on the $H-H_2O$ sites were assigned. All LJ parameters used for NbOFFIVE-1-Ni and guest H_2O molecules are given in Table S1. Each isotherm point was computed using 200,000 equilibration steps, followed by 500,000 production steps to achieve statistical convergence. Translation, rotation, reinsertion, and configurational bias swap (insertion/deletion) moves were applied in the simulations.

The saturated vapor pressure (p_0) for TIP4P water at 300 K was determined from bulk-phase transition matrix Monte Carlo (TMMC) simulations, as implemented in gRASPA. All force field parameters (atomic charges, Lennard−Jones parameters, tail corrections, and cutoffs) were identical with those used in the GCMC simulations. A cubic simulation box of $20 \times 20 \times 20$ Å^3 was used to satisfy the minimum image convention. The macrostate space (i.e., the number of molecules in the box, ranging from 0 to 300) was divided into intervals of 20 molecules (0−20, 21−40, ..., 280−320). A macrostate biasing scheme was applied to ensure sufficient sampling within each interval. For every interval, we used 12,000,000 Monte Carlo steps for equilibration, during which the biasing function was constructed, followed by 120,000,000 steps for production to generate the collection matrix. The biasing function was updated every 1,000,000 steps. The fugacity used in the TMMC simulations was chosen close to the transition fugacity (4700 Pa). Using the standard reweighting formula, the macrostate probability distribution (MPD) obtained from TMMC can be analytically reweighted to any other fugacity.[57,58] The MPD can also be used to compute the grand thermodynamic potential and, consequently, the corresponding pressure,[59] allowing for explicit conversion between fugacity and pressure. This relationship was used to convert pressures into fugacities for the corresponding GCMC simulations, as tabulated in Table S2. The saturated vapor pressure (p_0) for TIP4P water was calculated as 5197 Pa at 300 K. To present isotherms on a relative scale (i.e., as a function of relative humidity, RH), we used the simulated p_0 for simulated isotherms and the experimental p_0 (3600 Pa at 300 K) for experimental isotherms, following the procedure recommended in our previous study[60] to ensure meaningful comparison.

Note that MLIP is used only in the MD portion of the SR cycle. While the MLIP provides near-DFT accuracy for describing framework flexibility and properties such as metal−ligand polarization, adsorption thermodynamics also depend sensitively on the properties of the bulk fluid phase. First-principles descriptions of water are known to exhibit significant deviations in vapor−liquid coexistence behavior and saturation pressure from experiment, which can lead to inaccurate adsorption equilibria. As shown by Siepmann and co-workers,[61] DFT-based water models overestimate the heat of vaporization and misrepresent coexistence densities. In contrast, well-parametrized empirical models such as TIP4P reproduce these thermodynamic properties with reasonable fidelity. For this reason, we employed a hybrid strategy: the MOF dynamics are modeled using the DFT-quality MLIP to capture realistic structural flexibility, while the adsorbate−adsorbate and adsorbate−framework interactions in GCMC are treated using classical water models to ensure thermodynamically consistent adsorption equilibria. This combination leverages the strengths of each approach, providing a physically balanced description of both the host flexibility and water phase behavior. Knowing the vapor pressure of the water model is also necessary for plotting the isotherms using the reduced pressure, p/p_0.

2.5. Implementation of the Sorption-Relaxation Method

To enable adsorption modeling for flexible frameworks using the SR method, we developed MOF adsorption with framework flexibility (MOFAFF), a Python-based package designed to automate iterative MLIP-MD/GCMC simulation iterations. The required input files for MOFAFF include LAMMPS and gRASPA configuration files and an "input" file specifying key simulation parameters such as pressure, temperature, the number of sorption-relaxation (S−R) iterations, the MLIP file path, and DDEC06 charge data, as well as environmental variable settings to control simulation execution. Example input files and detailed usage instructions are available in our GitHub repository (provided at the end of the article).

In this study, we used the DFT-optimized NbOFFIVE-1-Ni·12H$_2$O structure (i.e., the fully hydrated structure with 12 water molecules per unit cell) as the starting configuration for the SR simulations. The SR workflow was performed at 300 K, with iteration between MLIP-MD and GCMC simulations. In the relaxation module of each iteration, an MLIP-MD simulation of 1 ps was conducted (refer to Section 2.3) to allow the framework to relax in response to the adsorbed water molecules. The final frame from the MLIP-MD trajectory was extracted and used as the input structure for the subsequent sorption module, where a GCMC simulation was conducted to adjust the number of adsorbed water molecules at the imposed fugacity. Throughout the SR iterations, each GCMC simulation employed the same number of equilibration (200,000) and production steps (500,000) to obtain the water uptake value for a given frame at a given temperature and humidity (refer to Section 2.4).

The DDEC06 partial charges for each atom used in the GCMC simulations were taken from the DFT-optimized NbOFFIVE-1-Ni·12 H$_2$O structure. An initial comparison of atomic partial charges between two randomly selected FPMD frames and the DFT-optimized structure showed negligible deviations (Figure S3), suggesting that the use of a single set of atomic charges was appropriate for the entire SR process. As an additional test including configurations with the most extreme energies, we analyzed six additional frames from the FPMD trajectory: three with energies near the average and three corresponding to the largest fluctuations. In the worst case, the standard deviation for individual atomic charges was 0.025 e, confirming that the charges are essentially independent of the instantaneous configuration of the framework (Figures S27 and S28).

At the end of each GCMC portion of the SR cycle, the final GCMC configuration (MOF plus water molecules) was used as the new initial configuration for the next MD portion of the cycle, allowing the framework to dynamically respond to changes in the water occupancy. In MOFAFF, to ensure compatibility between the relaxation and sorption stages, we made minor adjustments to the bond lengths and angles of water molecules extracted from the MLIP-MD frames to match the TIP4P model parameters (Figure S4). These modifications were minimal and preserved the relative spatial arrangement of the water molecules and their hydrogen-bonding networks. This MLIP-MD/GCMC loop was repeated for 100 iterations, corresponding to a total of 100 MLIP-MD simulations (each 1 ps) and 100 GCMC simulations (each with 200,000 equilibration and 500,000 production steps). The adsorption capacity was determined by averaging the water uptake over all of the iterations.

2.6. Experimental Methods

2.6.1. Synthesis of NbOFFIVE-1-Ni.
Nickel nitrate hexahydrate (175 mg, 0.6 mmol), niobium(V) oxide (79 mg, 0.3 mmol), pyrazine (384 mg, 4.8 mmol), and cesium fluoride (1.1 g, 3.3 mmol) were combined with 5 mL of deionized water in a Teflon bomb and thoroughly mixed for 10 min. Subsequently, 300 μL of concentrated nitric acid (68%) was added to the mixture before heating at 130 °C for 24 h. Upon cooling to room temperature, violet and white crystals formed. These crystals were washed with water and methanol three times to remove any remaining cesium fluoride (white crystals). Activation of NbOFFIVE-1-Ni was performed by degassing the methanol-washed sample under dynamic vacuum while heating at 105 °C for 24 h.

2.7. X-ray Diffraction Analyses

Powder X-ray diffraction (PXRD) patterns of the MOFs were collected at room temperature by using a STOE-STADIP powder
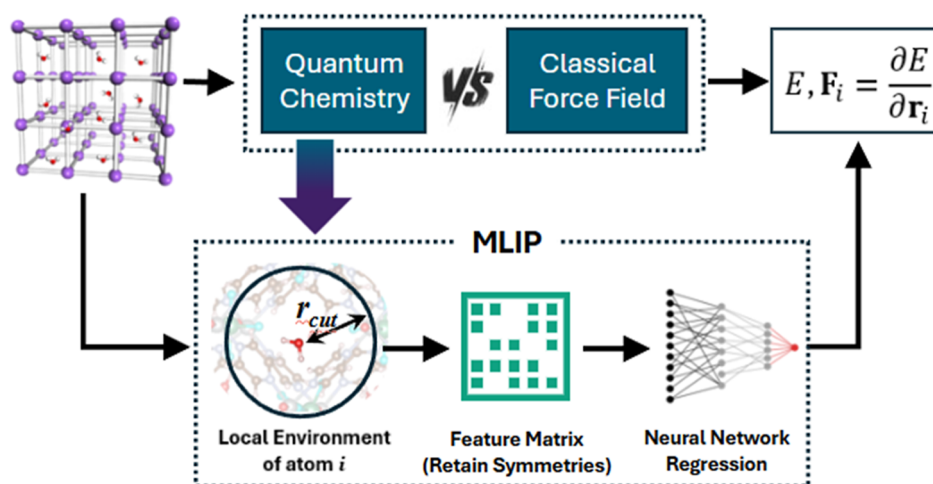
Figure 2. Schematic illustration of how the MLIP predicts the energy and forces for a given MOF configuration, effectively overcoming the computational cost limitations of quantum chemistry methods and the accuracy limitations of classical force field-based calculations.

diffractometer equipped with an asymmetric curved Germanium monochromator (utilizing CuKα1 radiation, λ = 1.54056 Å) and a one-dimensional silicon strip detector (MYTHEN2 1K from DECTRIS). The Cu X-ray source, with a line-focused beam, was operated at 40 kV and 40 mA. The powdered sample was placed between two Kapton sheets and analyzed in a transmission setup with a rotating holder.

To investigate the structural changes of NbOFFIVE-1-Ni upon water adsorption, the well-activated sample was placed in a sealed container with liquid water at room temperature, ensuring a 100% relative humidity environment. The sample was left under these conditions overnight, allowing sufficient time for water vapor adsorption and potential structural transformations. PXRD patterns were collected before and after exposure to water vapor. To quantitatively evaluate the changes in cell volume, the unit cell parameters of both well-activated and moisture-treated NbOFFIVE-1-Ni were refined using the cif file of as-synthesized NbOFFIVE-1-Ni[16] and the corresponding PXRD patterns before and after water adsorption in Materials Studio. The calculated volume change is approximately 0.7%.

2.8. Vapor Adsorption Isotherms

NbOFFIVE-1-Ni was activated at 105 °C under dynamic vacuum on a Smart VacPrep system for 24 h. The temperature was initially ramped to 80 °C at a rate of 5 °C/min and held for 30 min before increasing to 105 °C. The well-activated samples were then used for isotherm measurements. Water isotherms were collected by using a Micromeritics 3Flex instrument at 300 K.

3. RESULTS AND DISCUSSION

3.1. DFT Optimization of NbOFFIVE-1-Ni and NbOFFIVE-1-Ni·12H₂O

We conducted DFT structural optimizations on the NbOFFIVE-1-Ni framework to investigate its structural properties both in its dry state and when fully hydrated with 12 water molecules per unit cell (NbOFFIVE-1-Ni·12H₂O). Given the potential for different spin states at the nickel (Ni) centers, various magnetic orderings were systematically examined within the unit cell, including ferromagnetic, ferrimagnetic, and antiferromagnetic configurations, as depicted in Figure S5. The total energies corresponding to these configurations are summarized in Table S3. The results indicate that different magnetic orderings result in variations in total energy, regardless of water adsorption. However, the high-spin configuration, where all four Ni atoms align with spin

up, yielding a total magnetic moment of 8 μB, consistently exhibits energies that are very close to those of the lowest-energy spin states. The energy difference between high-spin and the lowest energy configuration is only 0.16 eV for NbOFFIVE-1-Ni (1.42 meV/atom) and 0.13 eV for NbOFFIVE-1-Ni·12H₂O (0.88 meV/atom). Since these energy differences are very small, we adopted the high-spin state in subsequent simulations to reduce the computational complexity.

The DFT-optimized lattice parameters for NbOFFIVE-1-Ni are $a = b$ = 9.82 Å and c = 15.74 Å, which are in excellent agreement with the experimental values of $a = b$ = 9.93 Å and c = 15.66 Å,[16] with deviations of 1.1% in the a and b directions and 0.5% in the c direction. Upon full hydration to NbOFFIVE-1-Ni·12H₂O, the DFT lattice parameters increase slightly to a = 9.85 Å, b = 9.89 Å, and c = 15.91 Å, leading to a unit cell volume expansion from 1518.65 Å³ to 1548.22 Å³, which corresponds to a minor increase of 1.9%. This slight volumetric change is consistent with experimental powder X-ray diffraction (PXRD) data (Figure S6), where the patterns for the dry and hydrated states remain nearly identical, with several peaks exhibiting slight shifts, particularly at 2θ = 23° and 26°, confirming that water adsorption induces minimal changes in lattice parameters and volume. This finding is consistent with previous work.[16]

In addition to minor changes in lattice parameters upon water adsorption, we also observed that the DFT-optimized geometry of NbOFFIVE-1-Ni·12H₂O exhibits linker distortions compared to that of the dry framework. To further investigate this effect, we manually rotated the organic linkers by 25° from their optimized orientations (Figure S7a) and performed DFT relaxations. In the absence of water, the linkers returned to their original positions, indicating that such distortions are energetically unfavorable. Similarly, when 12 water molecules were introduced into the framework, the initially distorted linkers also relaxed back to their original orientations (Figure S7b). However, the arrangement of the linkers is less ordered compared with the water-free counterpart, exhibiting a certain degree of distortion. Further quantitative analysis of these distortions is provided in Section 3.2.

E
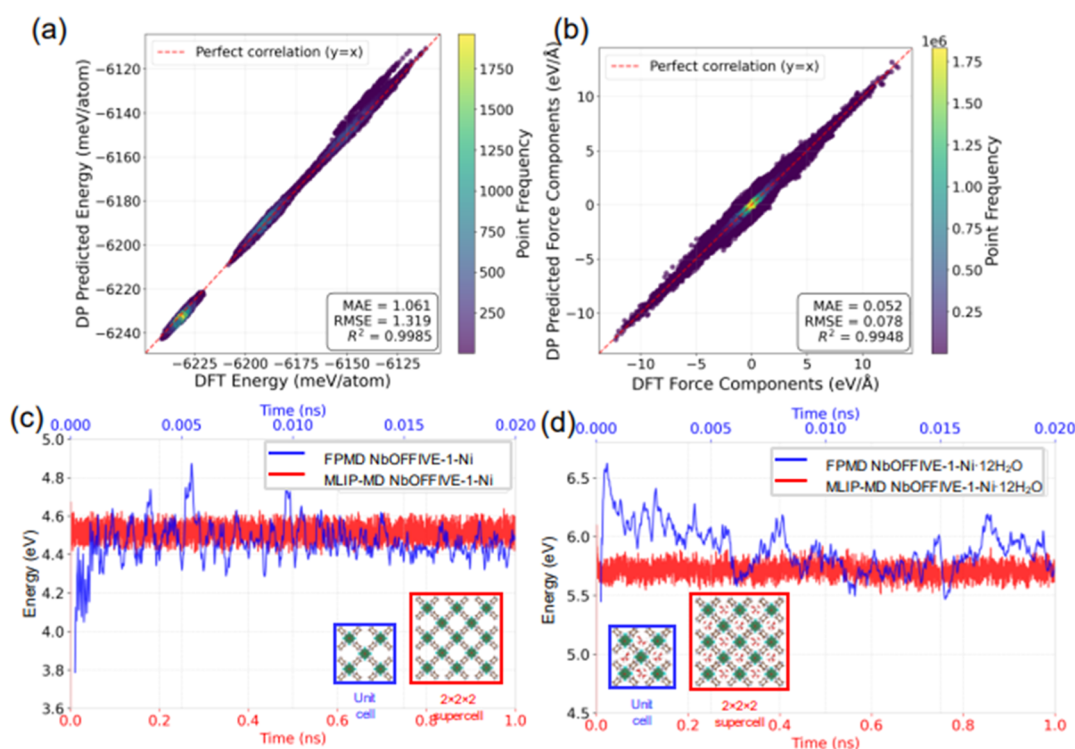
Figure 3. Parity plots, MAEs, and RMSEs of (a) energy and (b) forces for unseen testing data set of NbOFFIVE-1-Ni·12H$_2$O. DP stands for DeePMD-kit Potential. Training data: 20,000 FPMD frames at 300 and 600 K, along with 5000 FPMD frames starting from a manually twisted linker (25°); testing data: ~25,000 FPMD frames at 300, 600, and 900 K. (c) Moving average of energy per unit cell over time for FPMD (blue) of the NbOFFIVE-1-Ni unit cell and MLIP-MD (red) of the NbOFFIVE-1-Ni 2 × 2 × 2 supercell. (d) Moving average of energy per unit cell over time for FPMD (blue) of the NbOFFIVE-1-Ni·12H$_2$O unit cell and MLIP-MD (red) of the NbOFFIVE-1-Ni·12H$_2$O 2 × 2 × 2 supercell. The energy reference states are the DFT-optimized unit cells.

3.2. Training the MLIPs

To overcome the respective limitations of quantum chemistry and classical force fields, we adapted MLIPs to enable large-scale MD simulations with near-DFT accuracy. As illustrated in Figure 2, the MLIP was trained by extracting local environment information from atomic coordinates in the training data, projecting it onto a descriptor matrix, and then using a fitting neural network to predict the system's total energy and atomic forces (refer to Section 2.3 for more details). Here, we developed MLIPs for both NbOFFIVE-1-Ni and NbOFFIVE-1-Ni·12H$_2$O. The training data was generated using FPMD simulations conducted at 300 K, starting from the DFT-optimized geometries of NbOFFIVE-1-Ni and NbOFFIVE-1-Ni·12H$_2$O. Each simulation was performed for 20,000 steps with a 1 fs time step, capturing equilibrium structural fluctuations at room temperature. To expand the diversity of the training data set, additional FPMD simulations were performed using manually distorted structures, where the organic linkers were rotated by 25° from their optimized orientations (Figure S7). These simulations were run for 5000 steps at 300 K, revealing that the distorted linkers rapidly relaxed back to their original orientations within the first 300 steps. Although these distortions were short-lived, their inclusion in the training set ensured that the MLIP learned the system's response to these transient structural perturbations. To further enhance the robustness of the MLIP models, inspired by previous studies,[40] additional FPMD simulations were carried out at 600 K for 20,000 steps. At this elevated temperature, the increased thermal energy facilitated the sampling of a broader range of structural configurations. The

combined data set from equilibrium, distorted, and high-temperature simulations provided a diverse and comprehensive training set for the MLIPs. The data sets were then split into 80% training and 20% validation subsets for MLIP training (refer to Section 2.3 for training details).

The accuracy of the trained MLIPs was evaluated by analyzing parity plots, mean absolute errors (MAEs), and root-mean-square errors (RMSEs) for both energy and force predictions using an independently generated data set. This testing data set consisted of ~25,000 frames from the equilibrated portion of FPMD simulations of NbOFFIVE-1-Ni·12H$_2$O and NbOFFIVE-1-Ni at 300, 600, and 900 K using VASP 6.4.1. Note that some of the simulations did not finish due to run-time limits, so the frame number may be lower than 25,000 at a given temperature. As shown in Figure 3a,b for NbOFFIVE-1-Ni·12H$_2$O and in Figure S9 for NbOFFIVE-1-Ni, the MLIP-predicted energies and forces exhibit excellent agreement with the DFT reference values. The RMSEs with and without water were approximately 2 meV atom^{-1} for energies and below 0.1 eV Å^{-1} for atomic forces. Parity plots of energies and forces for each individual test temperature are provided in Figure S8 for NbOFFIVE-1-Ni·12H$_2$O and in Figure S10 for NbOFFIVE-1-Ni. For NbOFFIVE-1-Ni at 900 K, a few outliers appear in the energy predictions (Figure S10f); however, this does not affect the overall conclusions since the SR simulations were carried out at room temperature, and the MLIP is used here only to calculate forces in the MD simulations. We also note a slight systematic underestimation of energies at 300 K for NbOFFIVE-1-Ni·12H$_2$O (Figure S8a), which likely arises from the weighting scheme used during
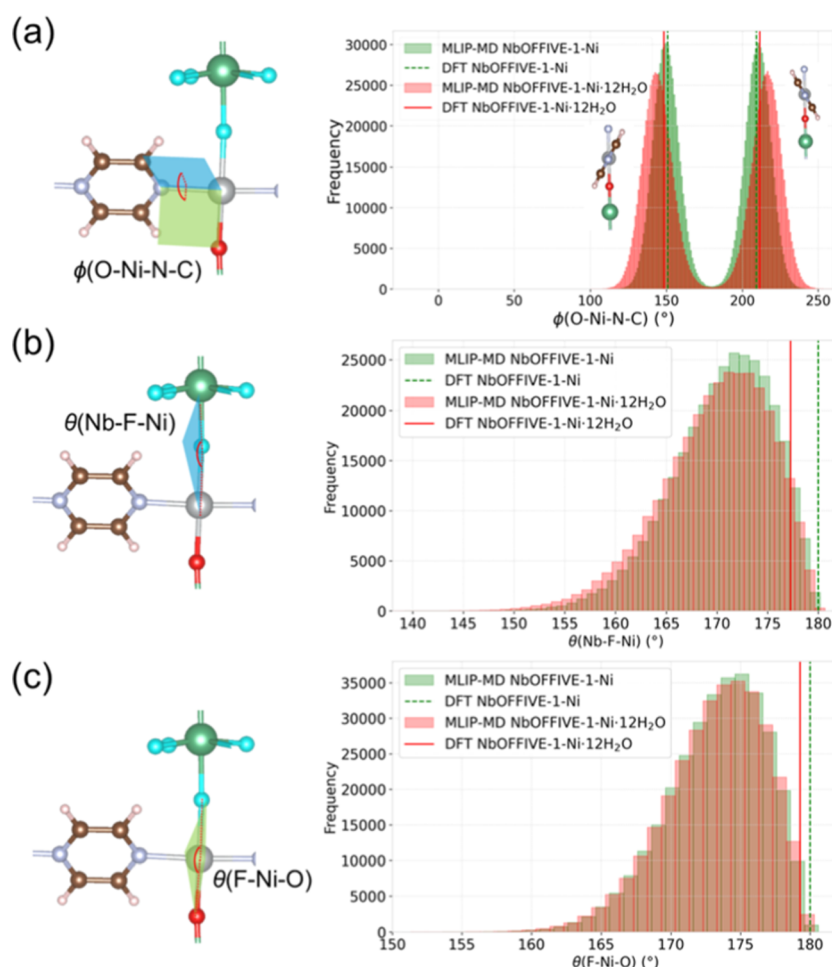
Figure 4. Schematic illustrations and frequency histograms of (a) $\phi(\text{O−Ni−N−C})$, (b) $\theta(\text{Nb−F−Ni})$, and (c) $\theta(\text{F−Ni−O})$ obtained from 1 ns MLIP-MD simulations for NbOFFIVE-1-Ni (green) and NbOFFIVE-1-Ni·12H$_2$O (red) 2 × 2 × 2 supercells. Atom colors: white (H), light blue (N), brown (C), red (O), cyan (F), silver (Ni), and green (Nb).

training, where the force and energy weights were set to 1000:0.02 at the start of the training to emphasize accurate force learning. Another possible reason is that the training set was generated using VASP 5.4.4, while the test set was generated using VASP 6.4.1, which may result in slight energy differences. Further improvements could be achieved by reducing large outliers through extended sampling and retraining, which would tighten the force and energy error distributions and improve the overall model robustness. Despite this bias, the RMSE remains below 2 meV atom^{-1}, well within the intrinsic accuracy of DFT. These results confirm that the trained MLIP reliably reproduces the energy and force landscapes of the framework structures.

To further assess the reliability of the MLIPs, MD simulations were performed on a 2 × 2 × 2 supercell of NbOFFIVE-1-Ni for 1 ns. The moving average of the energy per unit cell obtained from the MLIP-MD simulations closely matched the corresponding FPMD results for the initial 0.02 ns, with deviations of less than 0.1 eV (Figures 3c and S11a). Additionally, single-point DFT energy calculations were performed on randomly selected frames from the MLIP-MD trajectory. The energy differences per unit cell between MLIP predictions and DFT reference values remained below 0.005% (Table S4), confirming that the MLIP accurately reproduces the system's energy landscape. A similar validation was conducted for NbOFFIVE-1-Ni·12H$_2$O using the 2 × 2 × 2

supercell model. The moving average energy per unit cell obtained from MLIP-MD deviated from FPMD by only 0.3 eV (Figures 3d and S11b). Single-point DFT calculations on randomly selected MLIP-MD frames showed deviations of less than 0.03% (Table S5), further confirming that the MLIP model accurately predicts the energetics of the hydrated framework.

To assess the diversity of configurations sampled by MLIP-MD, we compared the energy variances from AIMD and MLIP-MD trajectories for one unit cell of NbOFFIVE-1-Ni and NbOFFIVE-1-Ni·12H$_2$O over 0.02 ns (Figure S12). The two methods exhibit comparable variance, indicating that MLIP-MD captures a configurational space similar to that of AIMD. For NbOFFIVE-1-Ni, the energy variance is 0.19 eV^2 for AIMD and 0.12 eV^2 for MLIP-MD, while for NbOFFIVE-1-Ni·12H$_2$O, the corresponding values are 0.23 eV^2 and 0.16 eV^2, respectively. Note that the apparent variances in Figure 3c,d are much smaller for MLIP-MD than for FPMD due to the different system sizes (1 versus 8 unit cells) since fluctuations scale with the square root of the number of atoms.

These validation results demonstrate that the trained MLIPs effectively model the structural dynamics and energetics of NbOFFIVE-1-Ni and NbOFFIVE-1-Ni·12H$_2$O, enabling efficient simulations on large systems, including 2 × 2 × 2 supercells containing 896 atoms for NbOFFIVE-1-Ni and 1184 atoms for NbOFFIVE-1-Ni·12H$_2$O. The MLIP-MD

G
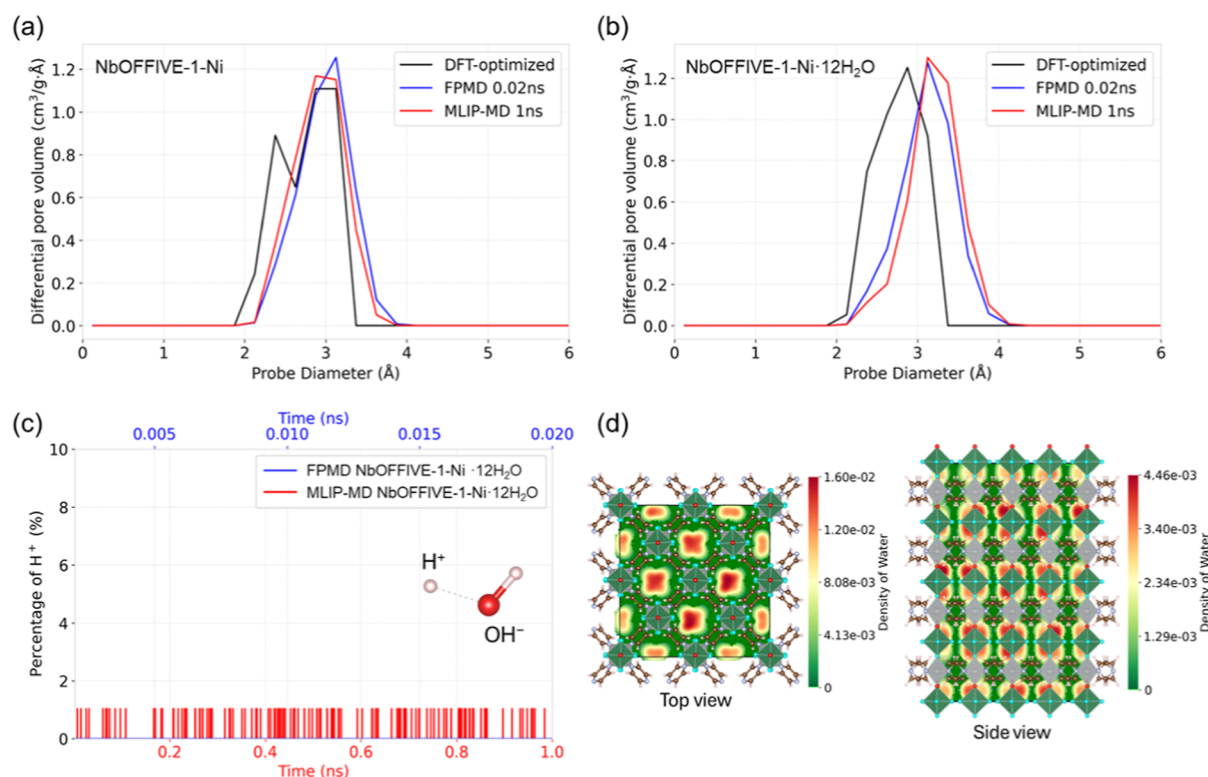
Figure 5. Pore size distributions of the (a) NbOFFIVE-1-Ni and (b) NbOFFIVE-1-Ni·12H$_2$O frameworks, computed from the DFT-optimized structures (black) and averaged over all frames from FPMD (blue, covering 0.02 ns) and MLIP-MD simulations (red, covering 1 ns with frames output every 100 simulation steps). Pore size distributions were obtained using PoreBlazer.[62] (c) Percentage of protons relative to water molecules over time from 0.02 ns FPMD simulations for the NbOFFIVE-1-Ni·12H$_2$O unit cell (blue) and 1 ns MLIP-MD simulations for the NbOFFIVE-1-Ni·12H$_2$O 2 × 2 × 2 supercell (red). The first 2 ps of each simulation were excluded to remove the equilibration portion of the simulation. A chemical bond between O and H is defined by d(O−H) < 1.1 Å. The blue line represents the FPMD result, which remains at zero throughout the simulation. (d) Density distribution of water molecules in the NbOFFIVE-1-Ni·12H$_2$O 2 × 2 × 2 supercell from MLIP-MD simulations, shown in top view (left) and side view (right). The color bar indicates the projected spatial density of O atoms from H$_2$O molecules in the respective planes, with units of atoms Å^{-2}. Atom colors: white (H), light blue (N), brown (C), red (O), cyan (F), silver (Ni), and green (Nb).

simulations achieved a computational speedup of 4 orders of magnitude compared to FPMD (refer to Table S6 for a summary of CPU times), allowing for nanosecond-scale simulations while maintaining DFT-level accuracy.

## 3.3. Impact of Adsorbed Water on Framework Flexibility

To investigate how water adsorption influences the structural flexibility of NbOFFIVE-1-Ni, we analyzed the geometric information obtained from MLIP-MD simulations of NbOF-FIVE-1-Ni and NbOFFIVE-1-Ni·12H$_2$O 2 × 2 supercells over 1 ns. Compared to the 0.02 ns FPMD simulations based on the unit cell model, the larger system size and extended simulation duration are expected to provide better sampling, thereby revealing more reliable information about water-induced framework flexibility.

We selected the ϕ(O−Ni−N−C) dihedral angles, ϕ(O−Ni−N−C), as descriptors to quantify the rotational motion of the organic linkers (Figure 4a, left). For each frame of the 2 × 2 × 2 supercell, there are 32 such dihedral angles, corresponding to 4 linkers per unit cell. In the DFT-optimized NbOFFIVE-1-Ni structure, dihedral angles of 150.7° and 209.3° (green dashed lines in Figure 4a, right) represent two distinct orientations of the linkers (180° ± 29.3°). After water adsorption, these angles shift slightly to 148.3° and 211.6° in the DFT-optimized NbOFFIVE-1-Ni·12H$_2$O structure (red solid lines). The distributions of ϕ(O−Ni−N−C) reveal that in the absence of water (green histogram), the linkers undergo

rotational motion but remain centered around the DFT-optimized angles. However, in the hydrated framework (red histogram), the peaks of the ϕ(O−Ni−N−C) distribution exhibit approximately 10° shifts, with one peak decreasing from 148.3° and the other increasing from 211.6°, suggesting that water enhances the rotational flexibility of the linkers.

Additionally, we examined the bending behavior of the metal node chains by analyzing two key bond angles: θ(Nb−F−Ni) and θ(F−Ni−O) (Figure 4b,c, left). In the DFT-optimized NbOFFIVE-1-Ni structure, both angles are precisely 180° (green dashed lines), indicating perfectly linear node chains. Upon water adsorption, the DFT-optimized NbOFFIVE-1-Ni·12H$_2$O structure exhibits only minor bending, with θ(Nb−F−Ni) decreasing to 177.9° and θ(F−Ni−O) to 179.6° (red solid lines in Figure 4b,c, right). For both dry and hydrated frameworks (green and red histograms), the distributions of θ(Nb−F−Ni) and θ(F−Ni−O) angles are very similar, with the θ(Nb−F−Ni) distribution centered around 172° and occasionally bending down to 150° and the θ(F−Ni−O) distribution centered around 174° with occasional bending down to 160°. This indicates that water adsorption has a negligible impact on the bending of the metal node chains at 300 K within the simulated time scale.

As a comparison, we also examined the distributions of ϕ(O−Ni−N−C), θ(Nb−F−Ni), and θ(F−Ni−O) obtained from the shorter 0.02 ns FPMD simulations of the unit cell model (Figure S13). Although the general trends for ϕ(O−
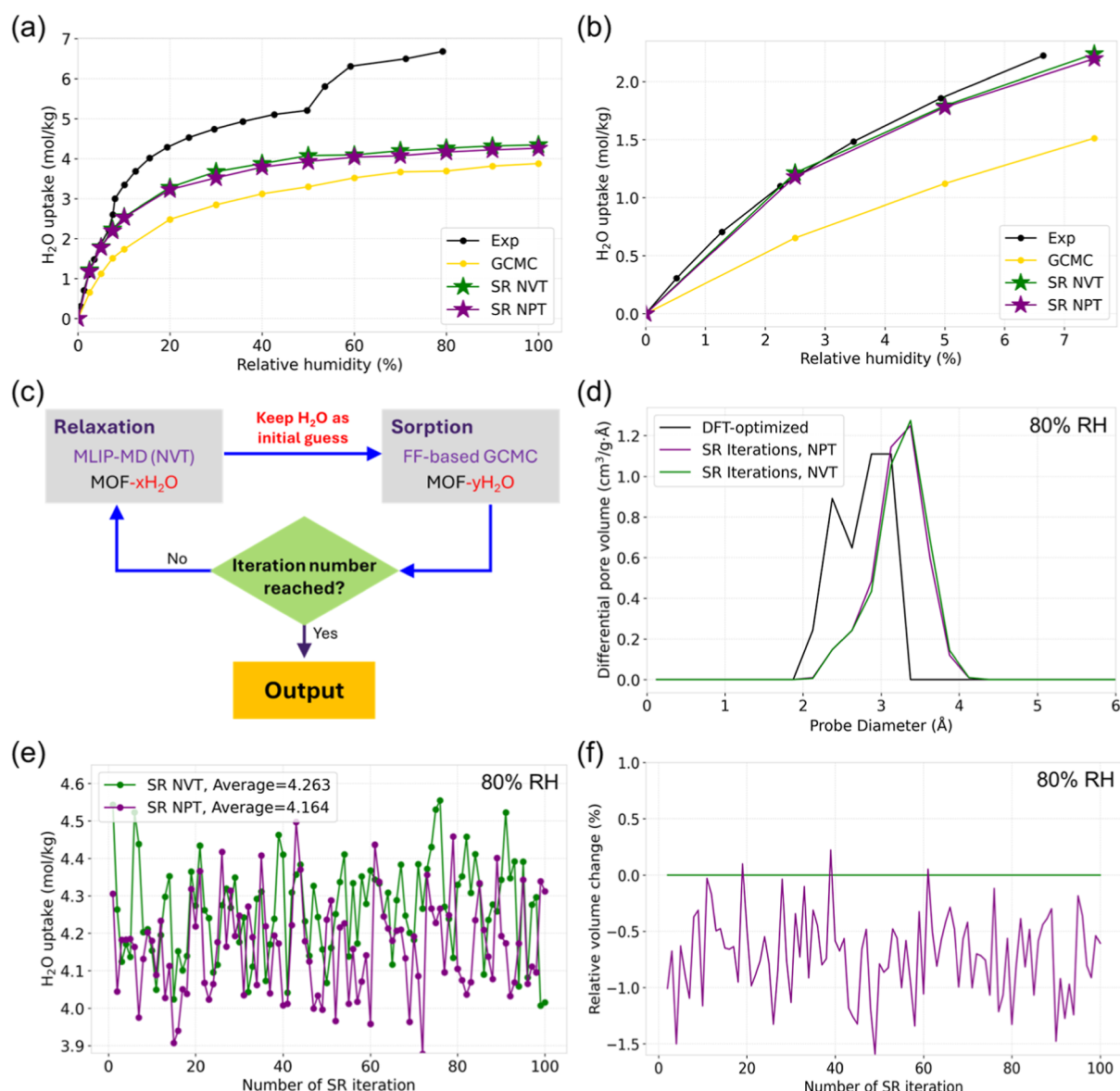
Figure 6. H_2O adsorption isotherms of NbOFFIVE-1-Ni at 300 K in the range of (a) 0−100% RH and (b) low RH (0−7.5%), obtained from background-corrected experimental data (black; see Figure S18 for more details), GCMC with rigid framework (yellow), and the SR approach with the MLIP-MD simulations in the *NVT* (green) and *NPT* (purple) ensembles. Each SR-derived data point represents the average H_2O uptake over 100 SR iterations. (c) Schematic illustration of the SR approach. (d) PSD of the NbOFFIVE-1-Ni framework at 80% RH computed from the DFT-optimized structure (black) and averaged over the final frames from each MLIP-MD simulation in the *NVT* (green) and *NPT* (purple) ensembles across 100 SR iterations. (e) H_2O uptake versus SR iteration at 80% RH, comparing the MLIP-MD simulations in the *NVT* (green) and *NPT* (purple) ensembles. (f) Percentage volume change over the SR iterations at 80% RH, with the MLIP-MD simulations in the *NVT* (green) and *NPT* (purple) ensembles.

Ni−N−C) and θ(F−Ni−O) are consistent with the MLIP-MD results, the distribution curves are noisier, potentially due to the limited system size and simulation time scale (Figures S14−S16). This observation highlights the importance of employing larger supercells and longer time scales to reduce statistical noise.

Next, we examined the impact of water molecules on the pore size distribution (PSD). We first analyzed the PSD of NbOFFIVE-1-Ni in its dry state by comparing the PSD of the DFT-optimized structure to the averaged PSDs obtained from FPMD and MLIP-MD simulations. For FPMD, the PSD was averaged over all frames generated during the 0.02 ns simulation. For MLIP-MD, the PSD was averaged over all output frames collected from a 1 ns simulation, where frames

were recorded every 100 simulation steps. As shown in Figure 5a, both FPMD and MLIP-MD sampling yielded similar PSD profiles (with a single peak spanning 2.8−3.1 Å), which differed notably from that obtained using the DFT-optimized structure (with a sharp peak at 2.4 Å and a broader peak from 2.8 to 3.1 Å). A similar contrast between the DFT-optimized structure and the MD-derived PSD profiles is observed for NbOFFIVE-1-Ni·12H$_2$O (Figure 5b), where the dominant pore diameter from the DFT-optimized structure is 2.8 Å, which is significantly lower than the values obtained from FPMD (3.1 Å) and MLIP-MD (3.1−3.5 Å). Comparing the MLIP-MD results (red curves) in Figure 5a,b further reveals an increase in the pore size upon water loading, suggesting that the dynamic interactions between water molecules and the

framework lead to pore expansion, highlighting the critical role of host−guest interactions in governing the structural properties of the material.

We further investigated the behavior of water molecules within the pores of NbOFFIVE-1-Ni, including the potential for proton (H^+) and hydronium ion (H_3O^+)[63] formation. By examining structural frames from both FPMD and MLIP-MD trajectories, we quantified the occurrence of water dissociation events leading to proton formation (Figure 5c). FPMD simulations indicated that no proton formation was observed throughout the simulation. Conversely, MLIP-MD simulations, which encompassed larger system sizes and extended time scales, occasionally exhibited a minimal fraction (<2%) of transiently dissociated protons. These protons rapidly recombined with hydroxide ions (OH^-) to reform water molecules, resulting in no long-lived ionic species and, thus, no impact on the results. Additionally, no H_3O^+ ion was observed in either the FPMD or MLIP-MD simulations (Figure S17). It would be interesting to train the MLIP with dissociated water states in future work, but this is beyond the scope of the current paper since it is unlikely that water dissociation plays a role in the adsorption process. We also examined the spatial density distribution of water molecules within the NbOFFIVE-1-Ni pores. The results indicate that due to the small pore size (diameter <4 Å), water molecules interact strongly with the framework, resulting in a near-uniform distribution within the confined spaces (Figure 5d).

3.4. Impact of Framework Flexibility on Water Adsorption

As shown in Figure S18, the experimentally measured water adsorption isotherm at 300 K (black circles) exhibits a type I profile at low relative humidity (RH ≤ 7.5%), indicating microporous behavior. A noticeable adsorption step is observed around 7.5% RH, followed by an increase in uptake up to approximately 5.4 mol/kg at 50% RH. Beyond this point, a second adsorption step occurs, with the uptake continuing to rise and eventually surpassing 7 mol/kg at higher RH values.

Compared with the previously reported isotherm[16] (gray circles in Figure S18), our results show excellent agreement. Notably, both results exhibit adsorption steps at 7.5% and ~50% RH. However, we observed that background adsorption from external surfaces and the sorption tube is significant in this system. Therefore, to more accurately capture the intrinsic water uptake behavior of NbOFFIVE-1-Ni, we focus our subsequent discussion on the isotherm correction for background adsorption. Details of the background measurement and correction procedure are provided in the Supporting Information; see Figure S18.

To model water adsorption, we first attempted conventional rigid-framework GCMC simulations using the DFT-optimized NbOFFIVE-1-Ni structure. The resulting water adsorption isotherm (Figure 6a,b, yellow line) is significantly lower than our experimental values, consistent with previously reported simulation results.[18] Inspired by this prior work,[18] we also explored water uptake using the DFT-optimized framework structure from NbOFFIVE-1-Ni·12H$_2$O to account for the structural changes induced by water loading. As shown in Figure S19, H_2O loading can modify the framework structure, leading to increased water uptake; however, the uptake values remain lower than the experimental data. Additionally, as described in the caption of Figure S19, we sampled two different H_2O arrangements using short MC simulations in the *NVT* ensemble, which produced distinct framework deforma-

tions and resulted in varying water uptake values. These findings highlight the importance of developing a sampling approach that can adequately capture diverse configurations of the MOF when evaluating water uptake.

Recognizing the importance of water distribution in governing framework flexibility and its impact on water uptake behavior, we also applied the SR approach, which iteratively integrates the relaxation and sorption modules, as illustrated in Figure 6c. The relaxation module employs MLIP-MD simulations to account for framework flexibility. To ensure the MLIP model's reliability across different hydration states, we trained a third version of the MLIP with the training data set expanded beyond the original FPMD data for NbOFFIVE-1-Ni and NbOFFIVE-1-Ni·12H$_2$O. Additional data corresponding to 30,000 steps of FPMD simulations at both 300 and 600 K for unit cells with 0, 4, 8, and 12 H$_2$O molecules (denoted as NbOFFIVE-1-Ni·nH$_2$O, where n = 0, 4, 8, and 12) were incorporated. This expansion of the training data ensures that the final MLIP model accurately captures the adsorption behavior across a range of hydration levels. The MLIP's performance over the independent test set described in Section 3.2 is shown in Figures S20−S22, where the RMSEs for the total energy per unit cell remain below 10^{-2} eV, and those for atomic forces are less than 0.1 eV/Å. As in Section 3.2, we see an underestimation in the energies. However, since the forces are more important than energies in MD, we consider the model as well trained. After each MD portion of the SR cycle, the sorption module employs GCMC simulations to determine the water adsorption capacity, using as input the framework structure and configuration of water molecules from the final frame of the relaxation module. In the SR workflow, the relaxation and sorption modules are executed iteratively to provide a more realistic representation of dynamic water adsorption, incorporating both framework relaxation and variations in water loading (see Section 2.5 for more details).

While hybrid MD/MC approaches have been employed previously to account for framework flexibility in adsorption simulations with classical force fields,[64,65] the present MLIP-driven workflow differs fundamentally in both fidelity and scope. By incorporation of a DFT-quality machine learning interatomic potential, the MLIP-MD module in our SR workflow captures near-first-principles energetics for thousands of atoms, enabling direct sampling of linker rotations and subtle framework distortions that empirical force fields cannot reproduce. This integration bridges the gap between quantum accuracy and statistical sampling, allowing us to probe how collective yet small (≈5−10°) linker rotations modulate water binding and pore accessibility in NbOFFIVE-1-Ni.

Using the SR approach, we calculated the average water uptake over 100 SR iterations at each RH in the *NVT* ensemble for the MLIP-MD simulations (green line in Figure 6a). We additionally examined the *NPT* ensemble for the MLIP-MD simulations (purple line), where the pressure was held constant at each humidity level, allowing the framework volume to dynamically adjust. The two adsorption isotherms were nearly identical, with the *NPT* results showing slightly lower water uptake than *NVT* at high humidity levels. Notably, the water uptake values from the SR approaches (both *NVT* and *NPT*) more closely match the experimental isotherm, especially at low loadings, compared with the rigid-framework GCMC simulations based on the DFT-optimized structure (yellow line) across all studied humidity levels. This improvement can be attributed to framework relaxation and the

resulting pore expansion, as evidenced by the larger average pore sizes in the SR-sampled framework structures compared to the DFT-optimized structure, as shown in Figures S23 and 6d for low (10%) and high (80%) humidity levels, respectively. Despite the nearly perfect agreement with experimental data at low (<7.5%) RH (Figure 6b) and the improved water uptake estimations at higher RH compared to GCMC simulations using a rigid framework, the SR results still fall below the experimental data above 7.5% RH. In particular, the SR isotherm fails to reproduce the two sharp uptake steps observed experimentally at 7.5% and 50% RH.

To better understand these discrepancies between simulation and experiment, we first examined whether the discrepancy might arise from too few SR iterations. Using 80% RH as a representative example, we plotted water uptake versus the number of SR iterations over 100 iterations. As shown in Figure 6e, both the *NVT* and *NPT* results fluctuated between 3.9 and 4.6 mol/kg, with no upward or downward trend, suggesting that the simulations have converged. The average loading for the *NVT* SR runs was 4.26 mol/kg, and that for the *NPT* SR runs was 4.16 mol/kg. To estimate error bars, we divided the data into 5 blocks, calculated the average within each block, and defined the error bar as

$2 \times \sqrt{\frac{1}{N} \sum x_i^2 - \left(\frac{1}{N} \sum x_i\right)^2}$,[66] where $N = 5$ is the number of blocks and x_i is the average value in the block i. The computed error bars for *NVT* and *NPT* were 0.01 and 0.06 mol/kg, respectively, indicating that the results from the two simulation methods are almost the same within statistical error. Moreover, increasing the number of SR iterations up to 4000 (Figure S24) did not change the simulation results.

We also explored the effect of other simulation choices. In the GCMC portion of the SR simulations, water molecules undergo translation, rotation, reinsertion, and swap (insertion/deletion) moves with equal attempt probability (25%) assigned to each move type. The acceptance rates for each move at low (10%) and high (80%) humidity levels are shown in Figure S26 and Table S7. Translation and rotation moves have an acceptance rate near 50% as expected, but the other move types have acceptance rates below 1%. To test whether adjusting the relative probabilities of attempting different moves can influence the GCMC results, we drastically reduced the attempt probabilities for translation and rotation moves, setting translation and rotation at 4.55% and reinsertion and swap at 45.45%. We then repeated the GCMC simulations for SR iteration #1 at both 10% and 80% RH. As shown in Tables S8 and S9, neither the acceptance rates nor the final average water uptake values showed any notable change.

A potential cause of the steps in the experimental adsorption isotherms is some sort of phase change, gate opening, defect formation, or other structural change in the MOF, or a sudden change in the structure of the adsorbed water molecules within the pores. Interestingly, the experimental PXRD patterns (Figure S6) do not show any major changes between the dry and fully hydrated states and only a minor (<2%) volume change. Also, the *NPT* simulations at 80% RH predict a volume change of less than 1.5% (Figure 6f). We tested whether adjusting the rate of volume change in the *NPT* MLIP-MD simulations, controlled by the barostat damping parameter, as illustrated in Figure S25, would affect the water uptake. At 80% RH, the average water uptake from the SR simulations remained virtually unchanged.

Uncovering the cause of the steps in the experimental isotherms will likely require additional experimental characterization. One could ask why the simulations did not predict any structural change in the MOF beyond local linker rotation. Consider, for example, the hypothesis that the steps are caused by water-induced defects such as a disruption in the node-linker connectivity. Such defects have been reported in other MOFs under humid conditions and may enhance local hydrophilicity,[67−69] thereby promoting abrupt water uptake. To predict such a structural change, MLIP would need to be trained on configurations exhibiting these defects. One could hypothesize some structures and include them in the FPMD training set or one could perform FPMD simulations at even higher temperatures, hoping that the defects might form spontaneously. It should be noted that the FPMD simulations were relatively short (20 ps). Also, they were performed at a constant volume. Adding FPMD simulations to the *NPT* ensemble or using deliberately larger or smaller unit cell volumes might allow structural transitions to be discovered without hypothesizing a particular type of structural transition. Enhanced sampling techniques such as metadynamics could be useful in such studies, and techniques such as umbrella sampling could be used to explore proposed structural transitions in FPMD simulations. These methods could facilitate the exploration of otherwise inaccessible regions of the potential energy landscape. By enriching the training data set with sufficiently sampled configurations, the resulting MLIP would be better equipped to capture rare events such as conformational rearrangements, phase transitions, or defect formation. Robust sampling during the SR simulations is also a challenge. Such advancements should lead to more robust and realistic predictions of water uptake driven by framework flexibility and help narrow the gap between simulation and experiment in the coming years. We also note the recent development of universal machine learning interatomic potentials (uMLIPs), which can be fine-tuned for MOFs. The present workflow could serve as a complementary approach to uMLIP-based MD simulations, enabling more accurate modeling of adsorption phenomena. In the long term, advances in uMLIP frameworks may further bridge the gap between simulation and experiment in predicting water uptake, driven by framework flexibility.

4. CONCLUSION

In this study, we developed a MLIP-driven approach to investigate the impact of framework flexibility on water adsorption in the MOF NbOFFIVE-1-Ni. By training MLIPs on FPMD data, we achieved nanosecond-scale simulations of large supercells with near-DFT accuracy and computational efficiency 4 orders of magnitude faster than FPMD. These simulations revealed that water adsorption significantly enhances the rotational flexibility of the organic linkers while leaving the rigidity of the metal node chains largely unaffected. This distinction highlights the critical role of linker dynamics in accommodating guest molecules within a flexible framework.

To accurately model adsorption in flexible MOFs, we developed a sorption-relaxation workflow that iteratively integrates MLIP-MD with GCMC simulations. This approach dynamically accounts for framework flexibility, leading to a more realistic description of water uptake compared with conventional rigid-framework GCMC simulations. The resulting water adsorption isotherms exhibit improved agreement with the experimental data measured in our lab. While the SR

approach marks a clear step forward, it does not reproduce the two-step adsorption behavior observed experimentally at ~7.5% and ~50% relative humidity. This discrepancy suggests that certain structural phenomena, such as defect formation, gate-opening, or other conformational rearrangements, may contribute to the observed stepwise uptake but are not fully sampled in the current SR approach. Addressing this issue remains a challenge for future work to enable robust and general predictive modeling of adsorption in flexible porous materials for applications in water adsorption, molecular separation, and gas storage.

■ ASSOCIATED CONTENT

Data Availability Statement

Data set containing the original data and key input/output files for DeepMD-kit used in training the machine learning interatomic potentials is available at https://zenodo.org/records/15750252. The MOFAFF code for running the SR cycles is available at https://github.com/xwsci/mofaff.

Ⓢ Supporting Information

The Supporting Information is available free of charge at https://pubs.acs.org/doi/10.1021/acs.jpcc.6c00023.

> Detailed information on NbOFFIVE-1-Ni structural models and GCMC adsorption isotherms, partial charge analysis of FPMD snapshots, UFF parameters, spin orderings and relative energies, experimental PXRD, linker rotation effects, MLIP training and validation, computational cost comparisons, Ni−O distance and H_3O^+ formation analysis, PSD across different SR iterations, GCMC convergence in SR iterations, impact of initial water configurations on GCMC uptake, and comparisons of volume evolution and adsorption under NVT and NPT ensembles (PDF)

■ AUTHOR INFORMATION

Corresponding Author

Randall Q. Snurr − *Department of Chemical and Biological Engineering, Northwestern University, Evanston, Illinois 60208, United States;* ⓞ orcid.org/0000-0003-2925-9246; Email: snurr@northwestern.edu

Authors

Xijun Wang − *Department of Chemical and Biological Engineering, Northwestern University, Evanston, Illinois 60208, United States*

Xiaoliang Wang − *Department of Chemistry, Northwestern University, Evanston, Illinois 60208, United States;* ⓞ orcid.org/0000-0002-6501-1136

Xiaoyi Zhang − *Department of Chemical and Biological Engineering, Northwestern University, Evanston, Illinois 60208, United States;* ⓞ orcid.org/0009-0000-4278-7743

Zhao Li − *Department of Chemical and Biological Engineering, Northwestern University, Evanston, Illinois 60208, United States;* ⓞ orcid.org/0000-0001-5035-4614

Jiayang Liu − *Department of Chemical and Biological Engineering, Northwestern University, Evanston, Illinois 60208, United States*

Faramarz Joodaki − *Department of Chemical and Biological Engineering, Northwestern University, Evanston, Illinois 60208, United States;* ⓞ orcid.org/0000-0003-2592-8246

Kaihang Shi − *Department of Chemical and Biological Engineering, Northwestern University, Evanston, Illinois 60208, United States; Department of Chemical and Biological Engineering, University at Buffalo, The State University of New York, Buffalo, New York 14260, United States;* ⓞ orcid.org/0000-0002-0297-1746

Filip Formalik − *Department of Chemical and Biological Engineering, Northwestern University, Evanston, Illinois 60208, United States; Department of Micro, Nano and Bioprocess Engineering, Wroclaw University of Science and Technology, 50-370 Wroclaw, Poland;* ⓞ orcid.org/0000-0003-3981-3298

Omar K. Farha − *Department of Chemical and Biological Engineering, Northwestern University, Evanston, Illinois 60208, United States; Department of Chemistry, Northwestern University, Evanston, Illinois 60208, United States;* ⓞ orcid.org/0000-0002-9904-9845

Daniela Kohen − *Department of Chemistry, Carleton College, Northfield, Minnesota 55057, United States;* ⓞ orcid.org/0000-0001-7900-1660

Complete contact information is available at:
https://pubs.acs.org/10.1021/acs.jpcc.6c00023

Author Contributions

[#]X.W. and X.W. contributed equally to this work.

Notes

The authors declare the following competing financial interest(s): Omar Farha and Randall Snurr have financial interests in Numat, a startup company that is commercializing metal-organic frameworks.

■ REFERENCES

(1) Yaghi, O. M.; O'Keeffe, M.; Ockwig, N. W.; Chae, H. K.; Eddaoudi, M.; Kim, J. Reticular synthesis and the design of new materials. *Nature* **2003**, *423* (6941), 705−714.

(2) Sengupta, D.; Melix, P.; Bose, S.; Duncan, J.; Wang, X.; Mian, M. R.; Kirlikovali, K. O.; Joodaki, F.; Islamoglu, T.; Yildirim, T.; Snurr, R. Q.; Farha, O. K. Air-stable Cu (I) metal−organic framework for hydrogen storage. *J. Am. Chem. Soc.* **2023**, *145* (37), 20492−20502.

(3) Senkovska, I.; Bon, V.; Mosberger, A.; Wang, Y.; Kaskel, S. Adsorption and Separation by Flexible MOFs. *Adv. Mater.* **2025**, *37*, 2414724.

(4) Jiang, Z.; Xu, X.; Ma, Y.; Cho, H. S.; Ding, D.; Wang, C.; Wu, J.; Oleynikov, P.; Jia, M.; Cheng, J.; Zhou, Y.; Terasaki, O.; Peng, T.; Zan, L.; Deng, H. Filling metal−organic framework mesopores with TiO$_2$ for CO$_2$ photoreduction. *Nature* **2020**, *586* (7830), 549−554.

(5) Dolgopolova, E. A.; Rice, A. M.; Martin, C. R.; Shustova, N. B. Photochemistry and photophysics of MOFs: steps towards MOF-based sensing enhancements. *Chem. Soc. Rev.* **2018**, *47* (13), 4710−4728.

(6) Chen, O. I.; Liu, C. H.; Wang, K.; Borrego-Marin, E.; Li, H.; Alawadhi, A. H.; Navarro, J. A. R.; Yaghi, O. M. Water-enhanced direct air capture of carbon dioxide in metal−organic frameworks. *J. Am. Chem. Soc.* **2024**, *146* (4), 2835−2844.

(7) Bose, S.; Sengupta, D.; Rayder, T. M.; Wang, X.; Kirlikovali, K. O.; Sekizkardes, A. K.; Islamoglu, T.; Farha, O. K. Challenges and opportunities: Metal−organic frameworks for direct air capture. *Adv. Funct. Mater.* **2024**, *34* (43), 2307478.

(8) Zheng, Z.; Nguyen, H. L.; Hanikel, N.; Li, K. K. Y.; Zhou, Z.; Ma, T.; Yaghi, O. M. High-yield, green and scalable methods for producing MOF-303 for water harvesting from desert air. *Nat. Protoc.* **2023**, *18*, 136−156.

(9) Lin, H.; Yang, Y.; Hsu, Y. C.; Zhang, J.; Welton, C.; Afolabi, I.; Loo, M.; Zhou, H. C. Metal-organic frameworks for water harvesting and concurrent carbon capture: a review for hygroscopic materials. *Adv. Mater.* **2024**, *36* (12), 2209073.

(10) Carrington, E. J.; Dodsworth, S. F.; van Meurs, S.; Warren, M. R.; Brammer, L. Post-synthetic modification unlocks a 2D-to-3D switch in MOF breathing response: a single-crystal-diffraction mapping study. *Angew. Chem.* **2021**, *133* (33), 18064−18068.

(11) Siwaipram, S.; Bopp, P. A.; Keupp, J.; Pukdeejorhor, L.; Soetens, J. C.; Bureekaew, S.; Schmid, R. Molecular insight into the swelling of a MOF: A force-field investigation of methanol uptake in MIL-88B (Fe)−Cl. *J. Phys. Chem. C* **2021**, *125* (23), 12837−12847.

(12) Damron, J. T.; Ma, J.; Kurz, R.; Saalwächter, K.; Matzger, A. J.; Ramamoorthy, A. The influence of chemical modification on linker rotational dynamics in metal−organic frameworks. *Angew. Chem.* **2018**, *130* (28), 8814−8817.

(13) Luo, T.; Jeppesen, H. S.; Schoekel, A.; Bönisch, N.; Xu, F.; Zhuang, R.; Huang, Q.; Senkovska, I.; Bon, V.; Heine, T.; et al. Photocatalytic Dehalogenation of Aryl Halides Mediated by the Flexible Metal-Organic Framework MIL-53 (Cr). *Angew. Chem., Int. Ed.* **2025**, *64*, No. e202422776.

(14) Oktavian, R.; Goeminne, R.; Glasby, L. T.; Song, P.; Huynh, R.; Qazvini, O. T.; Ghaffari-Nik, O.; Masoumifard, N.; Cordiner, J. L.; Hovington, P.; Van Speybroeck, V.; Moghadam, P. Z. Gas adsorption and framework flexibility of CALF-20 explored via experiments and simulations. *Nat. Commun.* **2024**, *15*, 3898.

(15) Grenev, I. V.; Shubin, A. A.; Solovyeva, M. V.; Gordeeva, L. G. The impact of framework flexibility and defects on the water adsorption in CAU-10-H. *Phys. Chem. Chem. Phys.* **2021**, *23* (37), 21329−21337.

(16) Bhatt, P. M.; Belmabkhout, Y.; Cadiau, A.; Adil, K.; Shekhah, O.; Shkurenko, A.; Barbour, L. J.; Eddaoudi, M. A fine-tuned fluorinated MOF addresses the needs for trace CO$_2$ removal and air capture using physisorption. *J. Am. Chem. Soc.* **2016**, *138* (29), 9301−9307.

(17) Guo, M.; Wu, H.; Lv, L.; Meng, H.; Yun, J.; Jin, J.; Mi, J. A highly efficient and stable composite of polyacrylate and metal−

organic framework prepared by interface engineering for direct air capture. *ACS Appl. Mater. Interfaces* **2021**, *13* (18), 21775−21785.

(18) Daglar, H.; Keskin, S.; Snurr, R. Q. Exploring the Effect of Framework Flexibility on Water Adsorption in the Metal−Organic Framework NbOFFIVE-1-Ni Using Molecular Modeling. *J. Phys. Chem. C* **2024**, *128* (44), 18913−18922.

(19) Moghadam, P. Z.; Chung, Y. G.; Snurr, R. Q. Progress toward the computational discovery of new metal−organic framework adsorbents for energy applications. *Nat. Energy* **2024**, *9* (2), 121−133.

(20) Park, H.; Majumdar, S.; Zhang, X.; Kim, J.; Smit, B. Inverse design of metal−organic frameworks for direct air capture of CO$_2$ via deep reinforcement learning. *Digit. Discov.* **2024**, *3* (4), 728−741.

(21) Park, J.; Kim, H.; Kang, Y.; Lim, Y.; Kim, J. From data to discovery: recent trends of machine learning in metal−organic frameworks. *JACS Au* **2024**, *4* (10), 3727−3743.

(22) Wang, L.; Liu, S.; Ji, Z.; Wang, J.; Shi, Y.; Lv, W.; Lu, X. Efficient CO$_2$ capture over N$_2$ in flexible MOFs: Pressure driven breathing effect. *Chem. Eng. Sci.* **2024**, *299*, 120562.

(23) Garcia-Perez, E.; Serra-Crespo, P.; Hamad, S.; Kapteijn, F.; Gascon, J. Molecular simulation of gas adsorption and diffusion in a breathing MOF using a rigid force field. *Phys. Chem. Chem. Phys.* **2014**, *16* (30), 16060−16066.

(24) Yu, Z.; Anstine, D. M.; Boulfelfel, S. E.; Gu, C.; Colina, C. M.; Sholl, D. S. Incorporating Flexibility Effects into Metal−Organic Framework Adsorption Simulations Using Different Models. *ACS Appl. Mater. Interfaces* **2021**, *13* (51), 61305−61315.

(25) Schaper, L.; Keupp, J.; Schmid, R. Molecular dynamics simulations of the breathing phase transition of MOF nanocrystallites II: explicitly modeling the pressure medium. *Front. Chem.* **2021**, *9*, 757680.

(26) Kulichenko, M.; Nebgen, B.; Lubbers, N.; Smith, J. S.; Barros, K.; Allen, A. E. A.; Habib, A.; Shinkle, E.; Fedik, N.; Li, Y. W.; Messerly, R. A.; Tretiak, S. Data generation for machine learning interatomic potentials and beyond. *Chem. Rev.* **2024**, *124* (24), 13681−13714.

(27) Goeminne, R.; Vanduyfhuys, L.; Van Speybroeck, V.; Verstraelen, T. DFT-Quality adsorption simulations in metal−organic frameworks enabled by machine learning Potentials. *J. Chem. Theory Comput.* **2023**, *19* (18), 6313−6325.

(28) Vandenhaute, S.; Cools-Ceuppens, M.; DeKeyser, S.; Verstraelen, T.; Van Speybroeck, V. Machine learning potentials for metal-organic frameworks using an incremental learning approach. *npj Comput. Mater.* **2023**, *9*, 19.

(29) Yue, Y.; Mohamed, S. A.; Loh, N. D.; Jiang, J. Toward a Generalizable Machine-Learned Potential for Metal−Organic Frameworks. *ACS Nano* **2025**, *19* (1), 933−949.

(30) Li, Z.; Shi, K.; Dubbeldam, D.; Dewing, M.; Knight, C.; Vázquez-Mayagoitia, A.; Snurr, R. Q. Efficient implementation of Monte Carlo algorithms on graphical processing units for simulation of adsorption in porous materials. *J. Chem. Theory Comput.* **2024**, *20* (23), 10649−10666.

(31) Anstine, D. M.; Tang, D.; Sholl, D. S.; Colina, C. M. Adsorption space for microporous polymers with diverse adsorbate species. *npj Comput. Mater.* **2021**, *7* (1), 53.

(32) Anstine, D. M.; Colina, C. M. Sorption-induced polymer rearrangement: approaches from molecular modeling. *Polym. Int.* **2021**, *70* (7), 984−989.

(33) Dogan, E. B.; Maurin, G.; Ahunbay, M. G. Atomistic Insight into the Interfacial Structuring of ZIF-67 MOF/Polymer Composites and Their Propylene−Propane Adsorption Properties. *J. Phys. Chem. C* **2023**, *127* (41), 20491−20502.

(34) Kresse, G.; Furthmüller, J. Efficient iterative schemes for ab initio total-energy calculations using a plane-wave basis set. *Phys. Rev. B:Condens. Matter Mater. Phys.* **1996**, *54* (16), 11169.

(35) Blöchl, P. E. Projector augmented-wave method. *Phys. Rev. B:Condens. Matter Mater. Phys.* **1994**, *50* (24), 17953.

(36) Perdew, J. P.; Burke, K.; Ernzerhof, M. Generalized gradient approximation made simple. *Phys. Rev. Lett.* **1996**, *77* (18), 3865.

(37) Grimme, S.; Ehrlich, S.; Goerigk, L. Effect of the damping function in dispersion corrected density functional theory. *J. Comput. Chem.* **2011**, *32* (7), 1456−1465.

(38) Nosé, S. A unified formulation of the constant temperature molecular dynamics methods. *J. Chem. Phys.* **1984**, *81* (1), 511−519.

(39) Hoover, W. G. Canonical dynamics: Equilibrium phase-space distributions. *Phys. Rev. A:At., Mol., Opt. Phys.* **1985**, *31* (3), 1695.

(40) Zheng, B.; Oliveira, F. L.; Neumann Barros Ferreira, R.; Steiner, M.; Hamann, H.; Gu, G. X.; Luan, B. Quantum informed machine-learning potentials for molecular dynamics simulations of CO_2's chemisorption and diffusion in Mg-MOF-74. *ACS Nano* **2023**, *17* (6), 5579−5587.

(41) Balyakin, I. A.; Rempel, S. V.; Ryltsev, R. E.; Rempel, A. A. Deep machine learning interatomic potential for liquid silica. *Phys. Rev. E* **2020**, *102* (5), 052125.

(42) Upham, D. C.; Agarwal, V.; Khechfe, A.; Snodgrass, Z. R.; Gordon, M. J.; Metiu, H.; McFarland, E. W. Catalytic molten metals for the direct conversion of methane to hydrogen and separable carbon. *Science* **2017**, *358* (6365), 917−921.

(43) Wang, H.; Zhang, L.; Han, J.; Weinan, E. DeePMD-kit: A deep learning package for many-body potential energy representation and molecular dynamics. *Comput. Phys. Commun.* **2018**, *228*, 178−184.

(44) Zeng, J.; Zhang, D.; Lu, D.; Mo, P.; Li, Z.; Chen, Y.; Rynik, M.; Huang, L.; Li, Z.; Shi, S.; Wang, Y.; Ye, H.; Tuo, P.; Yang, J.; Ding, Y.; Li, Y.; Tisi, D.; Zeng, Q.; Bao, H.; Xia, Y.; Huang, J.; Muraoka, K.; Wang, Y.; Chang, J.; Yuan, F.; Bore, S. L.; Cai, C.; Lin, Y.; Wang, B.; Xu, J.; Zhu, J. X.; Luo, C.; Zhang, Y.; Goodall, R. E. A.; Liang, W.; Singh, A. K.; Yao, S.; Zhang, J.; Wentzcovitch, R.; Han, J.; Liu, J.; Jia, W.; York, D. M.; E, W.; Car, R.; Zhang, L.; Wang, H. DeePMD-kit v2: A software package for Deep Potential models. *J. Chem. Phys.* **2023**, *159*, 054801.

(45) Sours, T. G.; Kulkarni, A. R. Predicting structural properties of pure silica zeolites using deep neural network potentials. *J. Phys. Chem. C* **2023**, *127* (3), 1455−1463.

(46) Liang, W.; Zeng, J.; York, D. M.; Zhang, L.; Wang, H. Learning DeePMD-kit: A guide to building deep potential models. In *A practical guide to recent advances in multiscale modeling and simulation of biomolecules*; AIP Publishing; 2023.

(47) https://zenodo.org/records/15750252 (accessed June 27, 2025).

(48) Thompson, A. P.; Aktulga, H. M.; Berger, R.; Bolintineanu, D. S.; Brown, W. M.; Crozier, P. S.; in 't Veld, P. J.; Kohlmeyer, A.; Moore, S. G.; Nguyen, T. D.; Shan, R.; Stevens, M. J.; Tranchida, J.; Trott, C.; Plimpton, S. J. LAMMPS-a flexible simulation tool for particle-based materials modeling at the atomic, meso, and continuum scales. *Comput. Phys. Commun.* **2022**, *271*, 108171.

(49) Verlet, L. Computer" experiments" on classical fluids. I. Thermodynamical properties of Lennard-Jones molecules. *Phys. Rev.* **1967**, *159*, 98.

(50) Rappe, A. K.; Casewit, C. J.; Colwell, K. S.; Goddard, W. A., III; Skiff, W. M.; Skiff, W. M. UFF, a full periodic table force field for molecular mechanics and molecular dynamics simulations. *J. Am. Chem. Soc.* **1992**, *114* (25), 10024−10035.

(51) Boda, D.; Henderson, D. The effects of deviations from Lorentz−Berthelot rules on the properties of a simple mixture. *Mol. Phys.* **2008**, *106* (20), 2367−2370.

(52) Ewald, P. P. Die Berechnung optischer und elektrostatischer Gitterpotentiale. *Ann. Phys.* **1921**, *369* (3), 253−287.

(53) Manz, T. A.; Limas, N. G. Introducing DDEC6 atomic population analysis: part 1. Charge partitioning theory and methodology. *RSC Adv.* **2016**, *6* (53), 47771−47801.

(54) Limas, N. G.; Manz, T. A. Introducing DDEC6 atomic population analysis: part 4. Efficient parallel computation of net atomic charges, atomic spin moments, bond orders, and more. *RSC Adv.* **2018**, *8* (5), 2678−2707.

(55) Handel, R.; Davidchack, R. L.; Anwar, J.; Brukhno, A. Direct Calculation of Solid-Liquid Interfacial Free Energy for Molecular Systems: TIP4P Ice-Water Interface. *Phys. Rev. Lett.* **2008**, *100* (3), 036104.

(56) Vega, C.; Abascal, J. L. F. Simulating water with rigid non-polarizable models: a general perspective. *Phys. Chem. Chem. Phys.* **2011**, *13* (44), 19663−19688.

(57) Shen, V. K.; Errington, J. R. Metastability and instability in the Lennard-Jones fluid investigated by transition-matrix Monte Carlo. *J. Phys. Chem. B* **2004**, *108* (51), 19595−19606.

(58) Errington, J. R. Direct calculation of liquid−vapor phase equilibria from transition matrix Monte Carlo simulation. *J. Chem. Phys.* **2003**, *118* (22), 9915−9925.

(59) Siderius, D. W.; Hatch, H. W.; Errington, J. R.; Shen, V. K. Comments on "Monte Carlo simulations for water adsorption in porous materials: Best practices and new insights. *AIChE J.* **2022**, *68* (8), No. e17686.

(60) Formalik, F.; Chen, H.; Snurr, R. Q. Avoiding pitfalls in molecular simulation of vapor sorption: Example of propane and isobutane in metal−organic frameworks for adsorption cooling applications. *J. Chem. Phys.* **2024**, *160*, 184118.

(61) McGrath, M. J.; Siepmann, J. I.; Kuo, I.-F. . W.; Mundy, C. J. Vapor−Liquid Equilibria of Water from First Principles: Comparison of Density Functionals and Basis Sets. *Mol. Phys.* **2006**, *104* (22−24), 3619−3626.

(62) Sarkisov, L.; Harrison, A. Computational structure character-isation tools in application to ordered and disordered porous materials. *Mol. Simul.* **2011**, *37* (15), 1248−1257.

(63) Egan, C. K.; Paesani, F. Assessing many-body effects of water self-ions. II: H_3O^+ (H_2O) n clusters. *J. Chem. Theory Comput.* **2019**, *15* (9), 4816−4833.

(64) Rogge, J.; Goeminne, R.; Demuynck, R.; Gutiérrez-Sevillano, J. J.; Vandenbrande, S.; Vanduyfhuys, L.; Waroquier, M.; Verstraelen, T.; Van Speybroeck, V. Modeling Gas Adsorption in Flexible Metal−Organic Frameworks via Hybrid Monte Carlo/Molecular Dynamics Schemes. *Adv. Theory Simul.* **2019**, *2* (4), 1800177.

(65) Goeminne, R.; Krause, S.; Kaskel, S.; Verstraelen, T.; Evans, J. D. Charting the Complete Thermodynamic Landscape of Gas Adsorption for a Responsive Metal−Organic Framework. *J. Am. Chem. Soc.* **2021**, *143* (11), 4143−4147.

(66) Frenkel, D.; Smit, B. *Understanding Molecular Simulation: From Algorithms to Applications*, 2nd ed.; Academic Press: San Diego, 2002, pp 529−531.

(67) Liu, X.; Wang, X.; Kapteijn, F. Water and metal−organic frameworks: from interaction toward utilization. *Chem. Rev.* **2020**, *120* (16), 8303−8377.

(68) Todaro, M.; Buscarino, G.; Sciortino, L.; Alessi, A.; Messina, F.; Taddei, M.; Ranocchiari, M.; Cannas, M.; Gelardi, F. M. Decomposition process of carboxylate MOF HKUST-1 unveiled at the atomic scale level. *J. Phys. Chem. C* **2016**, *120* (23), 12879−12889.

(69) Zuluaga, S.; Fuentes-Fernandez, E. M. A.; Tan, K.; Xu, F.; Li, J.; Chabal, Y. J.; Thonhauser, T. Understanding and controlling water stability of MOF-74. *J. Mater. Chem. A* **2016**, *4* (14), 5176−5183.